Heliyon 10 (2024) e25586

Contents lists available at ScienceDirect

Heliyon

journal homepage: www.cell.com/heliyon

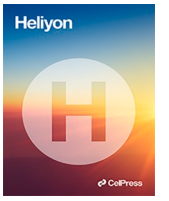

Research article

M-Ni-Co MOF (M=Zn, Fe, Mn) for high-performance supercapacitors by adjusting its morphology

Yige Yan [a], Mohan Huang [a], Yongsheng Wang [a], Dawei He [a,*], Jiaqi He [b]

[a] Key Laboratory of Luminescence and Optical Information, Ministry of Education, Institute of Optoelectronic Technology, Beijing Jiaotong University, Beijing, 100044, China
[b] College of Mathematics and Physics, Beijing University of Chemical Technology, Beijing, 100029, China

ARTICLE INFO

Keywords:
Metal-organic frameworks
Supercapacitors
Energy density
Morphology

ABSTRACT

Metal-organic frameworks (MOF) have been wildly synthesised and studied as electrode materials for supercapacitors, and bimetallic MOF of Ni and Co has been broadly studied to enhance both specific capacitance and stability of supercapacitors. Herein, a best performance (about 320 F/g) of Ni–Co bimetallic MOF was found in a uniform preparation condition by adjusting the ratio of Ni to Co. Then tiny third metal ion was introduced, and we found that the morphology of material has a significant change on the original basis. Furthermore, certain ions (Zn, Fe, Mn) introduced make a huge improvement in capacitance based on Ni–Co MOF of 320 F/g. The result shows that Zn–Ni–Co MOF, Fe–Ni–Co MOF and Mn–Ni–Co MOF perform specific capacitance of 1135 F/g, 870 F/g and 760F/g at 1 A/g, respectively. Meanwhile, the asymmetric supercapacitor (ASC) was constructed by Zn–Ni–Co MOF as positive electrode and active carbon (AC) as negative electrode. The Zn–Ni–Co MOF//AC ASC possesses a energy density of 58 Wh/kg at a power density of 775 W/kg. This research provides a new methods to regulate the morphology of MOF and a novel viewpoint for assembling high-performance, low-price, and eco-friendly green energy storage devices.

1. Introduction

With the ceaselessly consumption of non renewable energy, like fossil energy, the reserves of them reduce continuously. Renewable energy like wind, solar, power, etc, rapidly develop in this condition [1]. Therefore, the study of supercapacitors as a sort of energy storage devices is one of the key points to enhance the utilization rate of renewable energy [2]. Batteries with Faraday reaction as the main energy storage mechanism have properties of high energy density but low power density, while traditional capacitors with double layers as the main energy storage mechanism have properties of high power density but low energy density. The study and fabrication about supercapacitors aim to break through the power limit of batteries and energy limit of capacitors [3]. In addition, supercapacitors are used into some instruments which need both high power density and energy density, like electric vehicles, to make the vehicles more stable when they start or climb [4]. Supercapacitors are classified into three categories according to its energy storage mechanism, which are electric double layer capacitors (EDLCs), pseudocapacitors (PCs) and battery type capacitors (BTCs) [5]. Briefly, in EDLCs, the charge was stored by the reversible ion absorption at the interface between electrode and electrolyte [6]; in PCs,

* Corresponding author.
E-mail addresses: 22121683@bjtu.edu.cn (Y. Yan), 19118025@bjtu.edu.cn (M. Huang), yshwang@bjtu.edu.cn (Y. Wang), dwhe@bjtu.edu.cn (D. He), jqhe@mail.buct.edu.cn (J. He).

https://doi.org/10.1016/j.heliyon.2024.e25586
Received 23 November 2023; Received in revised form 28 January 2024; Accepted 30 January 2024
Available online 17 February 2024

the charge was stored by the redox reaction on or near the electrode surface [3]; in BTCs, redox reactions occurs in bulk phase of the active materials with the break and recombination process of chemical bond [3,7]. Materials about carbon was usually utilized into EDLCs, activated carbon (AC), carbon nanotubes (CNTs) and graphene included. They have disadvantage of low specific capacitance but advantages of high cycling stability, low cost, low toxicity and environmental friendliness [5,6]. On the contrast, PCs and BTCs can provide with high specific capacitance but a trivial cycling stability. RuO_2 is a classic material based on the surface redox reaction mechanism; MoO_3 is a typical material for BTCs, and MOF is a set of materials based on both redox reaction mechanism and double layer mechanism, which also be called hybrid supercapacitors (HSCs) [3,8,9].

MOF is a sort of materials that are constructed by the center and organic linkers. The center contains metal, and the strong bonds link the center and organic linkers. In this way, it grows into open crystalline frameworks with permanent porosity [10,11]. Varied metal salt and different organic linkers form thousands of types MOFs for different pore structures. High porosity makes MOF appropriate in adsorption, and varied pore structure make it high-performance in storage of different gas, like hydrogen, methane, acetylene, CO_2, etc [12–16]. High specific surface induced by the adjustable pore structures and ions in system supply MOF a high performance in supercapacitors [5,17]. The metal ions provide redox sites, while the porous structure and conjugated π electron cloud show the properties of double layers [18]. Notably, synergistic effect is a major factor to prove the electrochemical performance of electrodes [5]. For example, Garima Chaturvedi et al. synthesize a kind of nanoflower-like Ni-MOF material with a specific capacitance of about 815 F/g, and Yu Han et al. synthesize Co-MOF material with a specific capacitance of about 554.4 F/g, while Xiaoya Kang et al. Synthesize Ni, Co-MOF material with a specific capacitance of about 985.2 F/g [19,20]. Inducing a new metal ion may change the morphology of the material and increase the more binding sites, which make bimetallic MOF and trimetallic MOF widely be utilized into catalyzing [21].

In this work, a best ratio of Ni to Co was determined by a gradient experiment first. Base on the best ratio of Ni to Co, the third metal ion was introduced with different ratio to explore the influence on the capacitance and different morphology controlled by the third metal ion. And then, the best trimetallic MOF, Zn–Ni–Co with a certain ratio of Zn, was chosen to be the positive electrode of the ASC while AC was chosen to be the negative electrode. Zn–Ni–Co MOFs//AC ASC achieved a high energy density of 59.40 Wh/kg at a power density of 798 W/kg. Additionally, a method to control the morphology of MOFs was raised in this paper.

2. Experimental

2.1. Materials

Nickel chloride hexahydrate ($NiCl{\cdot}6H_2O$), cobaltous nitrate hexahydrate ($Co(NO_3)_2{\cdot}6H_2O$), zinc nitrate hexahydrate ($Zn(NO_3)_2{\cdot}6H_2O$), manganese nitrate tetrahydrate ($Mn(NO_3)_2{\cdot}4H_2O$), Ferric nitrate nonahydrate ($Fe(NO_3)_3{\cdot}6H_2O$), terephthalic acid (PTA) were obtained commercially (Shanghai Aladdin Reagent Co., LTD). N,N dimethylformamide (DMF) and Ethylene glycol (EG) was obtained by Modern Oriental (Beijing) Technology Development Co. Ltd.

2.2. Synthesis of Ni–Co-MOF

Certain amount of $NiCl{\cdot}6H_2O$, $Co(NO_3)_2{\cdot}6H_2O$ and 0.6 mmol PTA were dissolved into a mixed solution containing 20 mL DMF and 15 mL EG with the molar ratios (Ni: Co) of 0:1, 1:3, 1:1, 3:1 and 1:0. Samples of different molar ratio are presented by C-1 to C-5. The total amount of metal ions is 0.85 mmol. Subsequently, the solvend was ultrasonic dispersed for 10 min, followed by stirring for 2 h at room temperature to get a uniform bright red solution. Then, the solution was poured into reaction kettle, and the kettle was placed in oven at 170 °C for 6 h. After naturally cooling down to room temperature, the product was obtained by centrifugation. Finally, wash it with ethanol for three times and dry it at 60 °C for 12 h.

2.3. Synthesis of M-Ni-Co-MOF (M = Zn, Fe, Mn)

The third metal ion M^{n+} was added into Ni–Co-MOF in the first step. The total amount of Co and Ni was maintained, and the ratio (Co:Ni) of 1:1 was used in this synthesis process for its best electrochemical properties in the gradient ratio of bimetallic system. 0.425 mmol $Co(NO_3)_2{\cdot}6H_2O$, 0.425 mmol $NiCl{\cdot}6H_2O$, 0.6 mmol PTA and certain amount of M-salt were dissolved into a mixed solution containing 20 mL DMF and 15 mL EG with the molar ratios (Co:Ni:M) of 1:1:0.025, 1:1:0.05, 1:1:0.1, 1:1:0.15, 1:1:0.175. Samples of different ratio are represented by M − 1 to M − 5, respectively, where M = Zn, Fe, Mn. The rest process was the same as synthesis of Ni–Co-MOF's.

2.4. Electrochemical measurement

The electrochemical behavior of the samples as electrode materials for supercapacitors were performed on an electrochemical workstation (CHI660E, CH Instruments, Inc., Shanghai) with a representative three-electrode system at room temperature. The electrolyte was 2 M KOH aqueous solution; the counter electrode is platinum electrode, and reference electrode is Hg/HgO. In preparation of working electrode, the substance on the working contains 80 wt% active matter (about 4 mg Ni–Co or M-Ni-Co MOF), 10 wt% acetylene black as conductive agent, and 10 wt% polytetrafluoroethylene as binder. These matter were mixed into ethanol and coated onto a piece of nickel foam with an area about $1.0 \times 1.0\ cm^2$. Finally, the nickle foam was pressed with a pressure of 10.0 MPa to gain the working electrode. The active matter's mass was obtained by the mass discrepancy of nickle foam before and after pressing the

substance on. The electrochemical tests contains cyclic voltammetry (CV) at different scan rates from 5 mV/s to 50 mV/s, galvanostatic charging and discharging (GCD) at different current densities from 1 A/g to 20 A/g in voltage from 0 V to 0.4 V, and electrochemical impedance spectroscopy (EIS). According to the CV and GCD test, the specific capacitance (C, F/g) could be calculated by the following two equations [22,23]:

$$C = \frac{1}{2mv\Delta V}\int i(V)dV \tag{1}$$

$$C = \frac{I\Delta t}{m\Delta V} \tag{2}$$

Where C (F/g) is the specific capacitance of the working electrode, I (A) is the discharging current, t (s) is the discharging time, v (V/s) is the scan rate, and ΔV (V) is the potential window. To further understand the charge storage mechanism of a material as electrodes, chemical kinetics properties were analyzed through CV curve. It is well known that the correlation between different scanning rates v (V/s) and their corresponding peak current i (A) is shown in the following equation [24].

$$i = av^b \tag{3}$$

Generally, the storage mechanism of charge is judged by b value. The charge storage process tend to diffusion control which behavior more like batteries if the b value close to 0.5, while the charge storage process tend to surface capacitance control which behavior more like pseudocapacitors if the b value close to 1.0. Take the log of both sides of equation (3), we get equation

$$log\ i = b\ log\ v + log\ a \tag{4}$$

Value of b can be got form the slop of the line log(i) to log(v). Furthermore, the ratio of diffusion control and surface capacitance control can be determined by following equation [25].

$$i(v) = k_1 v + k_2 v^{1/2} \tag{5}$$

Where k_1v represents the degree offered by surface capacitance control, and k_2v represents the degree offered by surface diffusion control at different scan rate.

2.5. Material characterization

The micromorphology of samples were tested by scanning electron microscopy (SEM, SU8010, Hitachi, Japan) with an X-ray energy dispersive spectrometer (EDS). The crystal structure and chemical valence of the prepared materials were characterized by X-ray diffraction (XRD, Ultima IV, Cu Ka), and X-ray photoelectron spectroscopy (XPS, Thermo Scientific K-Alpha). Fourier transform infrared spectroscopy (FTIR) was conducted on a Spectrum One instrument (Frontier FTIR, PerkinElmer, USA).

2.6. Assembly of asymmetric supercapacitor (ASC)

Zn-3 pressed on the nickel foam as the positive electrode and active carbon on the nickel foam as the negative electrode, filter paper infiltrated by 6 M KOH as exchange membrane, an asymmetric supercapacitor (ASC) was assembled. The mass ratio of active materials Zn-3 and active carbon can be determined by following charge balance equation:

$$\frac{m^+}{m^-} = \frac{C_s^- \Delta V^-}{C_s^+ \Delta V^+} \tag{6}$$

where m (g) represents the mass of active materials in each electrode, C_s (F/g) is the specific capacitance of each active material as working electrode in a three electrode system, and V (V)is the potential window, the plus or minus sign represents that this physical quantity belongs to the positive electrode or the negative electrodes. Calculated by above equation, the ratio of active materials in positive electrode and negative electrode was 3.2: 1. The mass of Zn-3 was about 16 mg, and the mass of AC was about 5 mg in this work. After testing the electrochemical performance of ASC, the energy density (E, Wh/kg) and power density (P, W/kg) can be calculated by following equations:

$$E = \frac{1}{2 \times 3.6} C\Delta V^2 \tag{7}$$

$$P = \frac{3600 \times E}{\Delta t} \tag{8}$$

where C (F/g) is the specific capacitance determined by equation (1) or (2) of the assembled ASC, V (V) is voltage window of the ASC, and t (s) presents the discharging time in GCD curves.

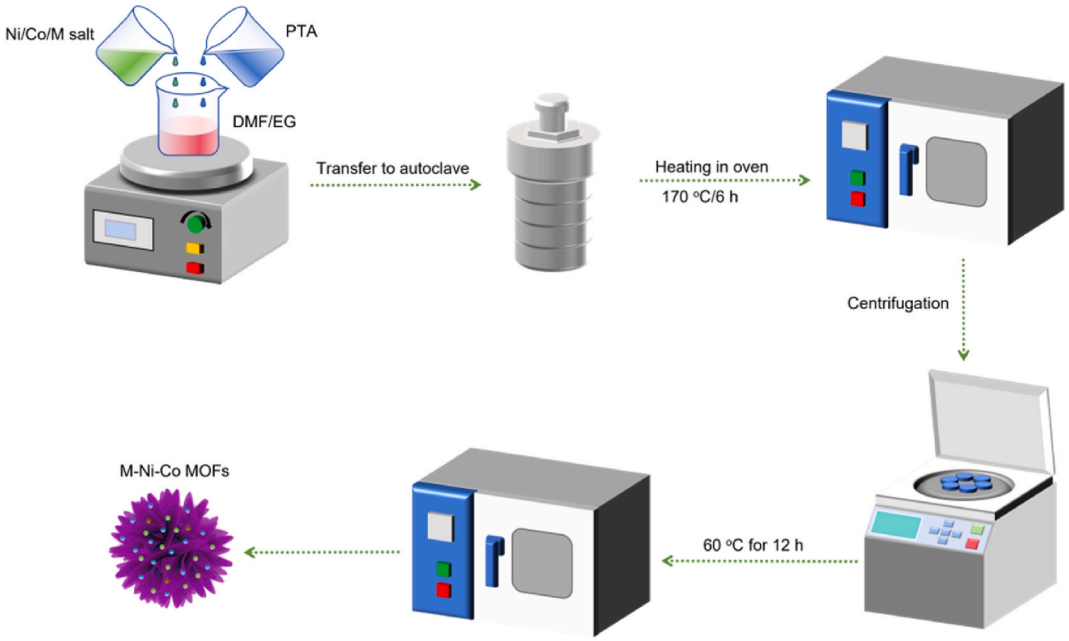

Fig. 1. Schematic illustration of the fabrication process of M-Ni-Co MOFs (M = Zn, Fe, Mn).

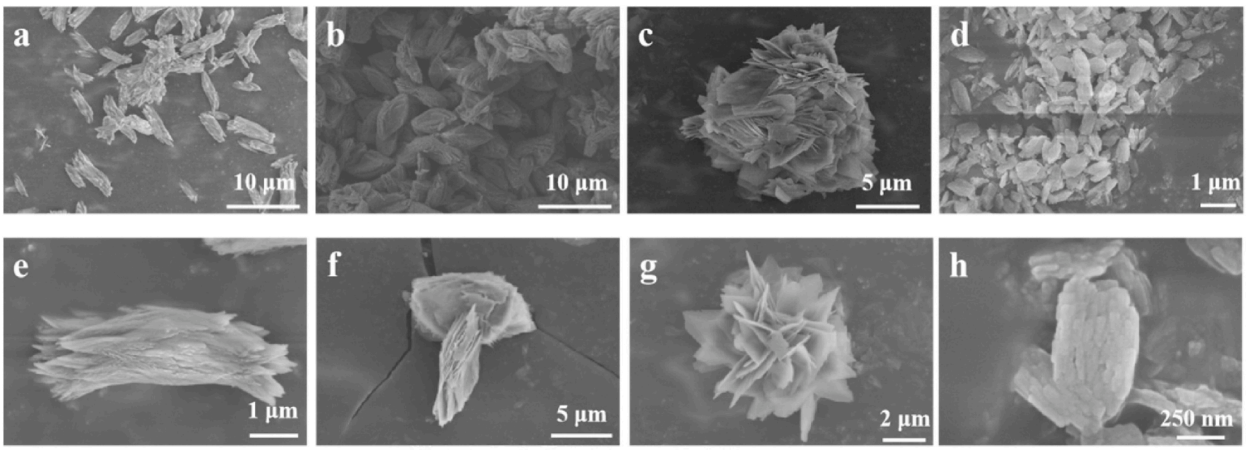

Fig. 2. The SEM images of (a, e) C-3, (b, f) Zn-3, (c, g) Fe-2 and (d, h) Mn-3.

3. Result and discussion

3.1. Structure and morphology characterization

The main synthesis procedure of M-Ni-Co MOF (M = Zn, Fe, Mn) was displayed in Fig. 1. Method of solvothermal was used. The morphology of C-3, Zn-3, Fe-2 and Mn-3 were analyzed by SEM. The images shown in Fig. 2a and e, the morphology of C-3 was microrob made of some tiny fibers (~700 nm), with a size about 5 μm long and 1.5 μm wide. Zn-3 (Fig. 2b and f) consist of boat-like unit with the size of about 6 μm long and 3 μm wide, and every unit was self-assembled by several sheets. As shown in Fig. 2c and g, the morphology of Fe-2 was microsphere made of some flakes (~1 μm), and the size is about 4~10 μm. Mn-3 (Fig. 2d and h) has a ellipsoidal particle structure, and every unit has a size of about 700 nm length and 350 nm width. The above description of dimensions was obtained by taking the average, and the statistical results were shown in Fig. S1 and S2. The introduction of a small amount of the third metal ion had a significant effect on changing the morphology of MOF. In addition, when the concentration of the third metal was appropriate, the morphology of the material tended to be uniform (Fig. 2 a, b and d). If the concentration of the third metal ion was too little, the morphology of the material tended to be complex. As shown in Fig. S3a, the morphology of Zn-1 included both microrob and boat-like structure. On the contrary, if the third metal ion is equivalent to Ni^{2+} and Co^{2+}, the morphology will tend to be irregular

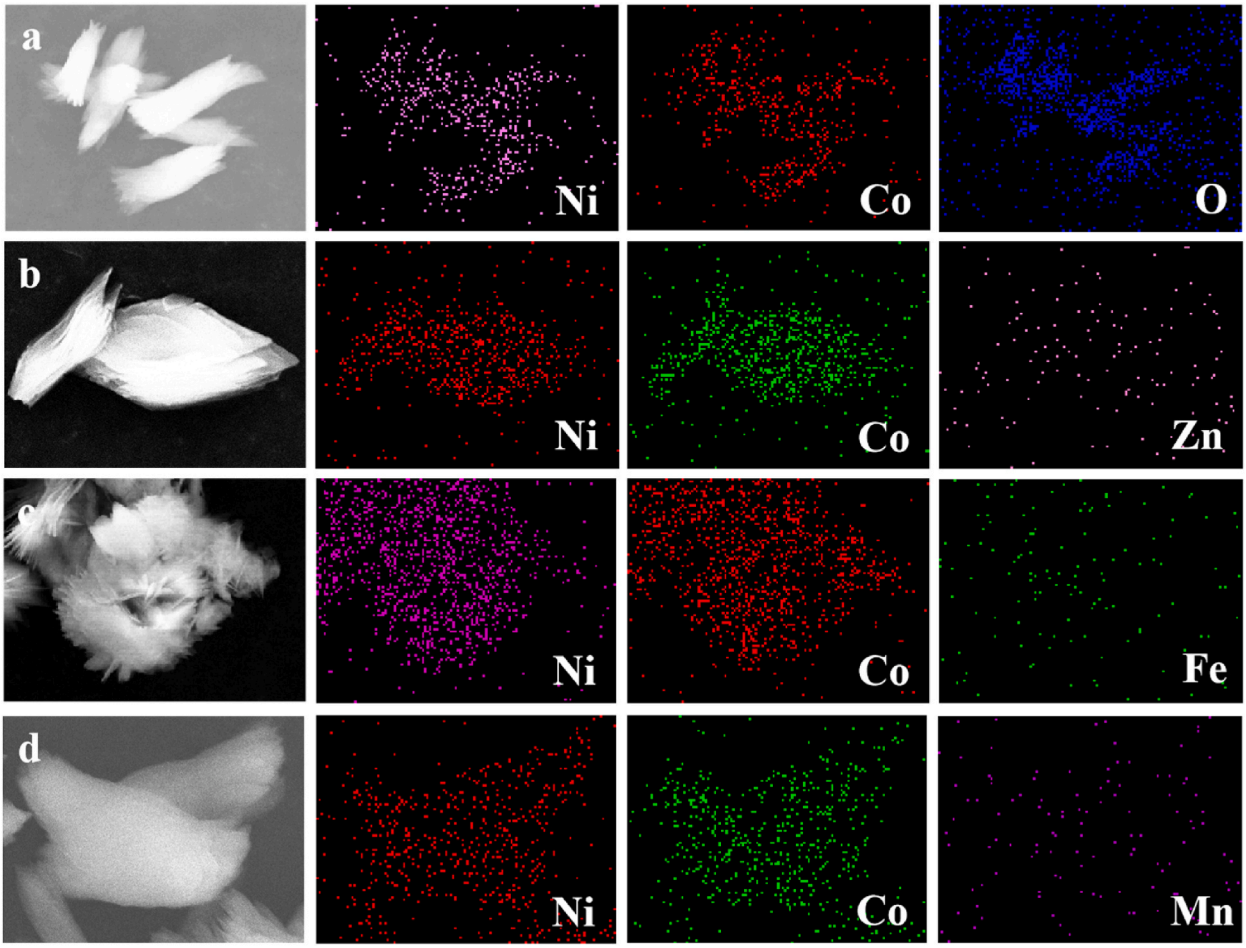

Fig. 3. The EDS mapping images for Ni, Co, O of C-3 (a), for Ni, Co, Zn of Zn-3 (b), for Ni, Co, Fe of Fe-2 (c) and for Ni, Co, Mn of Mn-3 (d).

(Fig. S3b), and there is a significant reduction in electrochemical performance. We believe that there must be a certain connection between morphology and electrochemical performance. Notably, in C-3, Zn-3 and Mn-3, the size of the units is similar to each other and separated from each other, while in Fe-2, the size of the microspheres is very different, and the spheres are easily cross-linked with others (Fig. S3c). This partly explains why C-3, Zn-3 and Mn-3 are powdery and Fe-2 is prone to agglomeration.

To explore the elements contained in samples, EDS mapping of C-3, Zn-3, Fe-2 and Mn-3 was performed and shown in Fig. 3. The images (Fig. 3ã d) shows that atomic ratio of Ni to Co was close to 1, and the report (Fig. S4c) also confirms this. Uniform dots in mapping images proved that Ni and Co indeed well doped in each sample. In C-3 (Fig. 2a), element O was also uniform and much more abundant than Ni and Co, which was one of the evidences proving that PTA was present in C-3 as organic ligands. In Zn-3, Fe-2, Mn-3 (Fig. 2b ~ d), The third metal atoms (Zn, Fe, Mn) was much less than Ni and Co, which was consistent with the synthesis procedure of M-Ni-Co-MOF. By Controlling for other variables in synthesis procedure, we believe that it is the third metal ion that caused the changes in morphology. As shown in Fig. S4, the atomic ratio of Ni, Co and M in sample Zn-3, Fe-2, Mn-3 were 8.86: 5.23: 0.01, 16.36: 14.83: 0.11 and 15.54: 14.10 and 0.22. The doping level of Zn is significantly lower than the other two group, which indicated that the doping level not only determined by the dose of ingredient. We speculate that Zn plays a role similar to that of a catalyst in the reaction process, participating in the process of changing morphology, but the actual number of coordination involved is very small.

The surface elemental composition and chemical state of C-3, Zn-3, Fe-2, Mn-3 were investigated by XPS. There are obvious peaks in the survey spectrum (Fig. 4a), proving that these four samples contain elements C, O, Ni and Co. The high-resolution XPS spectrum of C 1s (Fig. 4b) could be fitted with three characteristic peaks. Peak located at about 284.7 eV assigned to C–C, and the peaks at 286.3 and 288.4eV assigned to C–N and C═O, respectively [26,27,28], proving that the C is from organic ligands (C═O and C–C), and DMF (C–N and C–C). From the fitting result, the high-resolution XPS spectrum of Ni 2p (Fig. 4c) has two characteristic peaks which belong to Ni $2p_{3/2}$ and Ni $2p_{1/2}$ and two satellite peaks. According to the binding energy of 855.6 eV and 873.43 eV, the chemical state of Ni can be determined as Ni^{2+} [29–32]. Similarly, from the fitting result, the high-resolution XPS spectrum of Ni 2p (Fig. 4d) has two characteristic peaks which belong to Co $2p_{3/2}$ and Co $2p_{1/2}$ and two satellite peaks. According to the binding energy of 781.3 eV and 797.1 eV, the chemical state of Co can be determined as Co^{2+} [27,31–35]. Trace elements Zn, Fe, Mn were also analyzed in high-resolution XPS spectrum (Fig. 4e). In high-resolution XPS spectrum of Zn, peaks at 1021.3 and 1044.3 eV attribute to the typical characteristic

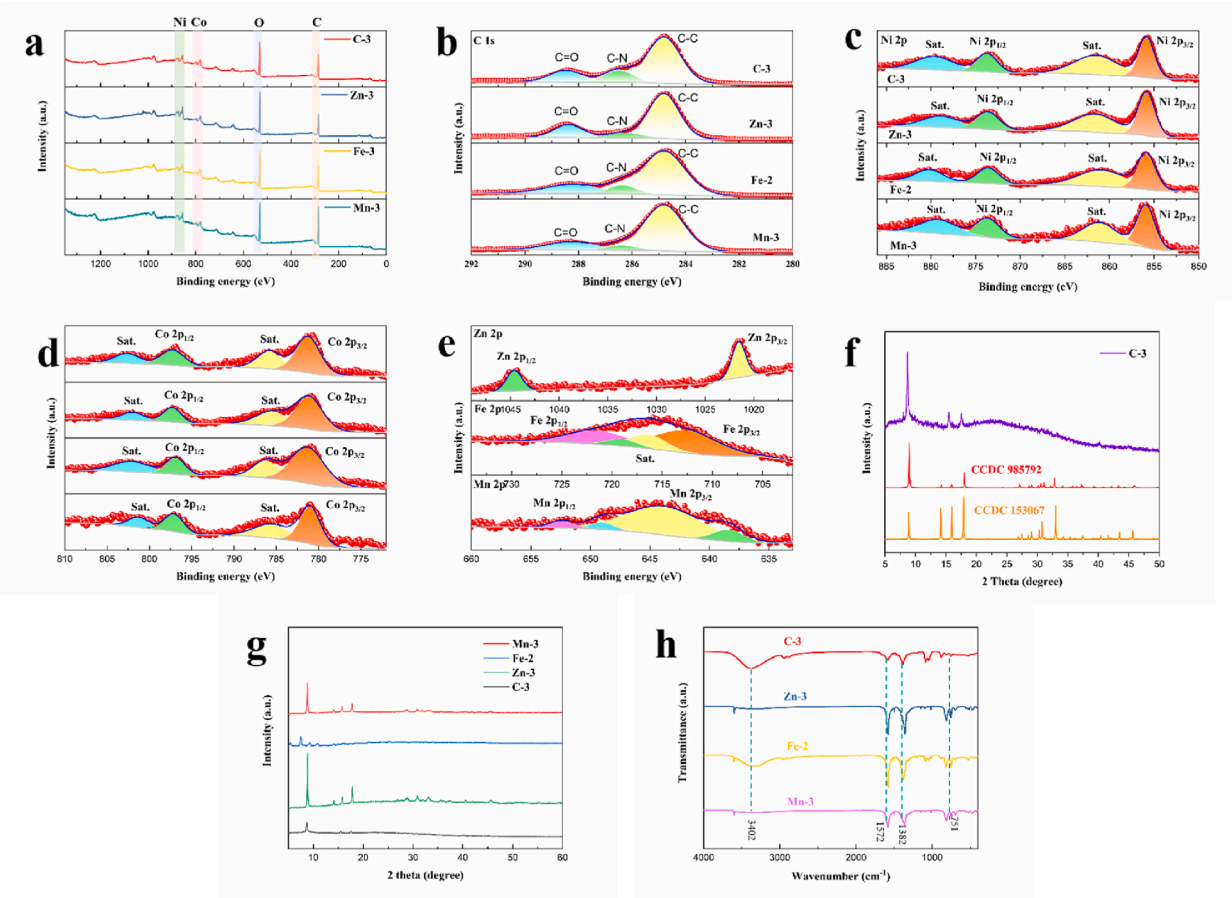

Fig. 4. (a) The XPS survey spectrum of C-3, Zn-3, Fe-2 and Mn. (b) C 1s, (c) Ni 2p, (d) Co 2p high-resolution XPS spectra of C-3, Zn-3, Fe-2 and Mn-3. (e) Zn 2p, Fe 2p and Mn 2p high-resolution XPS spectra of Zn-3, Fe-2 and Mn-3, respectively. (f) the XRD patterns of C-3 and standard cards. (g) the XRD patterns of C-3, Zn-3, Fe-2 and Mn-3. (h) The FTIR spectra of C-3, Zn-3, Fe-2 and Mn-3.

peaks of Zn^{2+} [36,37]. As for Fe, peaks at 712.3 eV and 723.4 eV can attribute to Fe $2p_{3/2}$ and Fe $2p_{1/2}$ orbitals, revealing that the valence state of Fe is Fe^{3+} [31,34,38–40]. The high-resolution XPS spectrum of Mn 2p could be fitted with four characteristic peaks, which located at 654.8 eV, 647.2 eV, 643.1 eV and 636.4 eV, and they can attribute to Mn $2p_{1/2}$, Mn^{2+}, Mn^{5+} and Mn^{3+} [41,42], indicating that Mn is unstable during high-temperature reaction, and some of it undergoes oxidation.

The crystallographic phase of C-3, Zn-3, Fe-2 and Mn-3 was characterized by XRD shown in Fig. 4f and g. As could be seen in Fig. 4f, the diffraction peaks of CCDC 153067 (Co-MOF) and CCDC 985792 (Ni-MOF) were very similar, which indicated that they have a very similar crystal structure. Besides, the characteristic peaks of C-3 located at $2\theta = 8.8°$, 15.7° and 17.8° were highly consist with the CCDC 153067 (Co-MOF) and CCDC 985792 (Ni-MOF) [43,44]. This indicated that the crystal structure of C-3 is similar to Ni-MOF and Co-MOF, which can be a strong evidence proving successful synthesis of Ni–Co MOF. Furthermore, Fig. 4g displayed the comparison of XRD patterns among C-3, Zn-3, Fe-2 and Mn-3. C-3, Zn-3 and Mn-3 had characteristic peaks located at the same degrees, indicating that they had similar crystal structure, while Fe-2 had different characteristic peaks, indicating that the crystal structure had changed. In order to further explore the changes in crystal structure of several MOFs, monometallic MOFs were synthesised at the same condition using the same ligand and tested in XRD, Zn-MOF, Fe-MOF and Mn-MOF included. As shown in Fig. S5a, Zn-MOF's characteristic peaks, Zn-3's characteristic peaks and C-3's characteristic peaks were highly matched indicating that they have similar crystal structures. The similarity of Zn-MOF's and C-3's characteristic peaks proves that changing the metal ion center of MOF from Ni^{2+} and Co^{2+} to Zn^{2+} has little impact on the crystal structure of MOF materials. This further explains the similarity between C-3's crystal structure and Zn-3's crystal structure. The XRD patterns of Fe-MOF, Fe-2 and C-3 were very different (Fig. S5b). The valence state of Fe is different from that of Ni and Co, which may cause the difference of coordination number, resulting in the changing of crystal structure. The differences among Fe-MOF's XRD pattern, Fe-2's XRD pattern and C-3's XRD pattern indicated that there can be certain cross action between Ni^{2+}, Co^{2+} and Fe^{3+} in Fe-2, leading to that the crystal structure of Fe-2 is different from that of Fe-MOF and that of C-2. Fig. S5c showed the XRD patterns of Mn-MOF, Mn-3 and C-3. Compering Mn-MOF and Mn-3 respectively to C-3, they have the same characteristic peaks at $2\theta = 8.8°$, 15.7° and 17.8°, while are different at interval from $2\theta = 20°$–35°. We believe that the complexity of valence state of Mn ion leads to this results. From the analysis of Fig. 4e, Mn^{2+}, Mn^{3+} and Mn^{5+} all existed in Mn-3 and

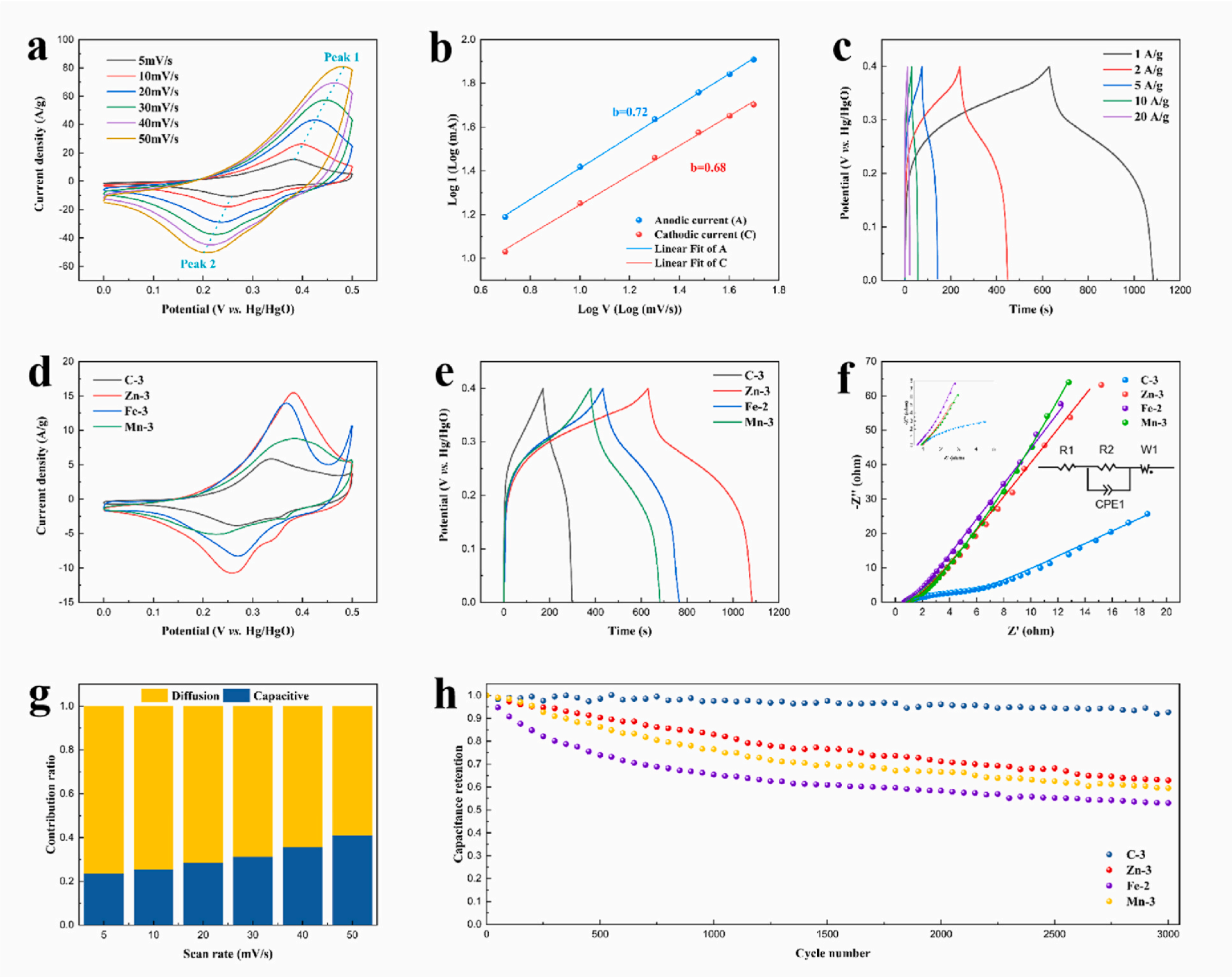

Fig. 5. (a) The CV curves at different scan rates of Zn-3. (b) Linear relation between logarithm of rates and logarithm of current peaks. (c) The GCD curves of Zn-3 at different current densities. (d) The CV curves at 5 mV/s and (e) the GCD curves at 1A/g of C-3, Zn-3, Fe-2 and Mn-3. (f) Nyquist plots of C-3, Zn-3, Fe-2 and Mn-3. (g) Different contribution ratios at different scan rates of Zn-3. (h) The cycling stability performance at 10 A/g for C-3, Zn-3, Fe-2 and Mn-3.

Mn-MOF. Mn^{2+} as the metal ion center may maintain its original crystal structure, while Mn^{3+} and Mn^{5+} very likely change the crystal structure, introducing new peaks into XRD pattern. According to the above analysis, we proposed two hypotheses regarding the mechanism by which the third metal ion affects morphology. First, the introduce of the third ion directly change the crystal structure of the MOF materials, resulting in the changing of the morphology. Second, the third metal ions do not change the crystal structure but change the lattice constant due to different atom size, affecting the self-assembly process, and then results in the change in morphology.

The surface chemical functional groups of C-3, Zn-3, Fe-2 and Mn-3 were analyzed by FTIR. As shown in Fig. 4h, the adsorption peak at 3402 cm^{-1} was a stretching vibration peak of O–H [45,46], representing the presence of coordinated H_2O molecules in these four samples. The adsorption peaks at about 1572 cm^{-1} and 1382 cm^{-1} can attribute to asymmetric and symmetric stretching modes of coordinated (–COO–) group [46], respectively, which was from organic ligands PTA. Additionally, The peak at 751 was derived from the bending vibrations of C–H, further confirming the existence of organic compounds in the materials.

3.2. Electrochemical performance of Ni–Co and M-Ni-Co MOF (M = Zn, Fe, Mn)

Before exploring the electrochemical performance of M-Ni-Co MOF materials, electrochemical performance of Ni–Co MOF materials containing different ratio of Ni to Co was test in a three-electrode system, 2 M KOH solution as electrolyte, in order to find a ratio of the best electrochemical performance. To emphasize the influence from different Ni, Co ratio, a working electrode used Ni–Co MOF prepared under the same condition with different ratio of Ni to Co. The galvanostatic chargedischarge (GCD) curves (Fig. S6a) of Ni–Co MOF (C-1 to C-5) showed that C-3 had the longest discharge time, which proved it had the highest charge storage capacity among Ni–Co MOF. Sample C-1 to C-5 have specific capacitance of 59.5 F/g, 185 F/g, 315 F/g, 268 F/g and 238 F/g respectively, according to

equation (2). Notably, the charging and discharging parts shows a nonlinear process with a plateau, which means that redox reactions occur in Ni–Co MOFs. As for C-3, cyclic voltammogram test was done with different scan rates from 5 to 50 mV/s (Fig. S6b). It is worth noting that obvious peaks existed in all CV curves, which can attribute to the redox reactions, and the plateaus in charging and discharging process of GCD curves also proved this reversible Faraday reactions. In addition, the oxidation peaks' position shift to positive orientation, and the reduction peaks positions shift to negative orientation with the increasing scan rate. This phenomenon can be ascribed to the influence of electrode polarization [17]. To further study the storage mechanism of charge, the relation between the logarithm of the current peaks and logarithm of the scanning rates is linearly fitted (Fig. S6c). The value of b was 0.79 for anodic current and 0.78 for cathodic current. Furthermore, the ratio of capacitance caused by diffusion control mechanism and caused by capacitance control mechanism was calculated by equation (5). Fig. S6d displayed this ratio at 5 mV/s to 50 mV/s In C-3, capacitance control dominated the whole charge storage process. As scanning rate increasing, surface-control's contribution lifted by degrees, while diffusion-control's contribution gradually declined. This result can attribute to the increased moving speed and of ions in the solution and ions' decreased diffusion path. In addition, as the scanning rates increasing, the ions in the solution was harder to reach internal part of the active materials, just staying at the interface between electrolyte and electrode. This process collaborated with polarization and ohmic effect to impeded the diffusion-control process and facilitated the surface-control process leading to the dominance of the suface-control process at a high scanning rate [23]. Fig. S6e was obtained by GCD testing of C-3 at different current densities ranging from 1 A/g to 20 A/g. By calculating, the specific capacitance values of C-3 were as large as 315 F/g, 302 F/g, 265 F/g, 220 F/g, 170 F/g at current densities of 1 A/g, 2A/g, 5 A/g, 10 A/g and 20 A/g, respectively. As the current density increased by 20 times, the capacitance of C-3 retained 52%. Furthermore, the GCD curves had a good symmetry with a pair of plateaus at different current densities proving that the Faraday reactions in charge storage process was highly reversible. Notably, when the current density reach to 20 A/g, GCD curve tended to linear indicating that redox reactions were unconspicuous, which proved that capacitance control dominated the charge storage process at huge charge density.

C-3 had the best electrochemical performance among C-1 to C-5, thus different ratio of ion M^{n+} (M = Zn, Fe, Mn) were introduced based on C-3, and they were called M − 1 to M − 5 according to different M concentration. Similarly, the electrochemical properties of each sample were studied by a three-electrode system in 2 M KOH aqueous electrolyte, and the working electrode used M-Ni-Co MOF. The CV curves of Zn–Ni–Co MOF (Zn-1 to Zn-5) (Fig. S7a) at 5 mV/s showed that Zn-3 had the largest integrated area, which indicated that Zn-3 had the largest specific capacitance among Zn–Co–Ni MOF, and GCD curves (Fig. S7b) at 1A/g also confirmed this by the longest discharge time for Zn-3. Calculated by equation (2), sample Zn-1 to Zn-5 had specific capacitance of 301 F/g, 610 F/g, 1135 F/g, 713.5 F/g and 488.5 F/g, respectively. As for Zn-3, cyclic voltammogram test was done with different scan rates from 5 to 50 mV/s (Fig. 5a). According to equation (4), value of b equals 0.72 for anodic current and 0.68 for cathodic current by linear fitting of log (i) and log (V) (Fig. 5b). Fig. 5c was obtained by GCD testing of Zn-3 at different current densities ranging from 1 A/g to 20 A/g. By calculating, the specific capacitance values of Zn-3 were as large as 1135 F/g, 1044 F/g, 863 F/g, 692 F/g, 522 F/g at current densities of 1 A/g, 2 A/g, 5 A/g, 10 A/g and 20 A/g, respectively. As the current density increased by 20 times, the capacitance of Zn-3 retained 46%. The CV curves (Fig. S8a) and GCD curves (Fig. S8b) of Fe–Ni–Co MOF (Fe-1 to Fe-5) showed that Fe-2 had the largest integrated area and longest discharging time, which proved that Fe-2 had the largest specific capacitance among Fe–Co–Ni MOF. According to equation (2), sample Fe-1 to Fe-5 have specific capacitance of 161 F/g, 835F/g, 167F/g, 107F/g and 52.5F/g, respectively. As for Fe-2, CV test was done with different scan rates from 5 to 50 mV/s (Fig. S8c). According to equation (4), value of b equals 0.67 for anodic current and 0.74 for cathodic current by linear fitting of log (i) and log (V) (Fig. S8d). Fig. S8e was obtained by GCD testing of Fe-2 at different current densities ranging from 1 A/g to 20 A/g. By calculating, the specific capacitance values of Fe-2 were as large as 835 F/g, 743 F/g, 635 F/g, 534 F/g, 426 F/g at current densities of 1 A/g, 2A/g, 5 A/g, 10 A/g and 20 A/g, respectively. As the current density increased by 20 times, the capacitance of Fe-2 retained 51%. Similarly, CV and GCD tests for Mn–Ni–Co was done. As shown in Fig. S9a and S9b, Mn-3 had the largest integrated area and longest discharging time, which proved that Mn-3 had the largest specific capacitance among Mn–Ni–Co MOF. According to equation (2), sample Mn-1 to Mn-5 have specific capacitance of 181.5 F/g, 318 F/g, 760 F/g, 297.5 F/g and 56.5 F/g, respectively. As for Mn-3, CV test was done with different scan rates from 5 to 50 mV/s (Fig. S9c). According to equation (4), value of b equals 0.60 for anodic current and 0.58 for cathodic current by linear fitting of log (i) and log (V) (Fig. S9d). Fig. S9e was obtained by GCD testing of Mn-3 at different current densities ranging from 1 A/g to 20 A/g. By calculating, the specific capacitance values of Mn-3 were as large as 760 F/g, 486 F/g, 319 F/g, 251 F/g and 122 F/g at current densities of 1 A/g, 2 A/g, 5 A/g, 10 A/g and 20 A/g, respectively. As the current density increased by 20 times, the capacitance of Mn-2 retained 16%. Additionally, the contribution of surface and capacitance controlled of Zn-3 (Fig. 5g), Fe-2 (Fig. S8f) and Mn-3 (Fig. S9f) at 5-50 mV/s was calculated by equation (5). Apparently, diffusion control parts of Zn-3, Fe-2 and Mn-3 were larger than that of C-3, and similar to C-3, the ratio of surface controlled gradually improved as the increase in scanning rates.

Fig. 5d showed CV curves of C-3, Zn-3, Fe-2 and Mn-3 which perform the best electrochemical properties in each group. Zn-3 had the largest integrated area consistent with its largest capacitance, and the longest discharging time (Fig. 5e) also confirmed this. To study the influence of various components of the electrode on its electrochemical performance, electrochemical impedance spectroscopy (EIS) of C-3, Zn-3, Fe-2 and Mn-3 was performed, and Nyquist plots of these four materials and equivalent circuit was shown in Fig. 5f. R2 in the equivalent circuit represented charge transfer resistance. By fitting, the R2 value of C-3, Zn-3, Fe-2 and Mn-3 were 4.07 Ω, 0.97 Ω, 0.67 Ω and 0.87 Ω. By contrast, the resistance of Zn-3, Fe-2 and Mn-3 is significantly smaller than C-3, which indicated that Zn-3, Fe-2 and Mn-3 had much faster charge transfer rates explaining their better electrochemical performance. Compared to some other Ni, Co-MOF or MOF derived LDT, R2 values of our samples still has advantages [16,17,22]. Table. S1 listed their R2 values. The cyclic stability of C-3, Zn-3, Fe-2 and Mn-3 was tested by charging and discharging cycles at current density of 10 A/g. As shown in Fig. 5h, after 3000 cycles, the specific capacitance retention rates of C-3, Zn-3, Fe-2, Mn-3 were 93 %, 63 %, 53 % and 60 %, respectively. The first and last 10 cycles of cycling stability test were displayed in Fig. S10. C-3 is more stable than other three. We

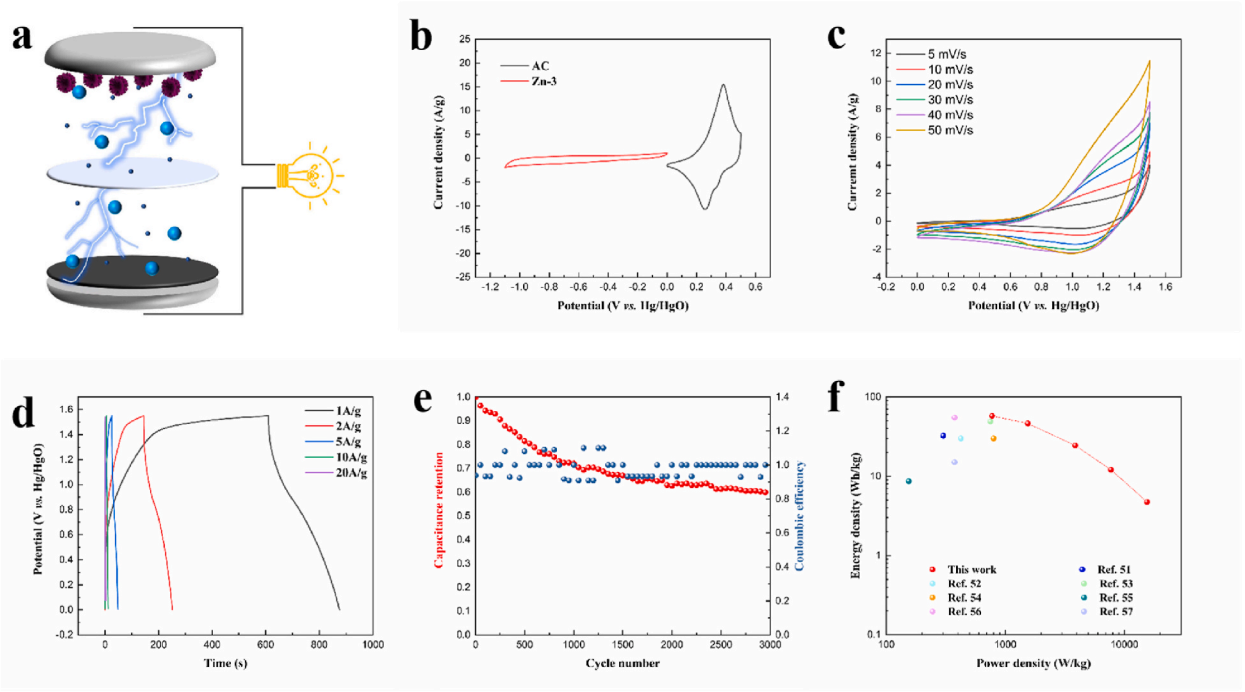

Fig. 6. (a) Schematic illustration of Zn-3//AC hybrid supercapacitor. (b) The CV curves of Zn-3 and AC electrodes at a scan rate of 5 mV/s in a three-electrode mode. Electrochemical performance of Zn-3//AC hybrid supercapacitor: (c) the CV curves at different scan rates from 5 mV/s to 50 mV/s, (d) the GCD curves at current densities from 1A/g to 20 A/g, (e) the cycling stability performance of Zn-3//AC HSC at a current density of 10 A/g. (f) The ragone plot correlating E and P compared with other reported hybrid devices.

speculated that the structure formed by introduction of new ions is not as stable as the structure of Ni–Co MOF, resulting in a lower stability than C-3's. Furthermore, numerous studies have shown that Ni-MOF and Co-MOF are unstable in alkaline solutions and form corresponding hydroxides [47–51]. This is one of the reasons why the cycling stability performance of Ni–Co MOF and M-Ni-Co MOF is much worse than Ni–Co layered double hydroxide (LDT) [22]. The redox reaction mechanism of Ni Co hydroxides was inferred from the above electrochemical characteristics and literature [22], and can be described as the following chemical equation:

$$Co(OH)_2(II) + OH^- \leftrightarrow CoOOH(III) + e^- \quad (9)$$

$$Ni(OH)_2(II) + OH^- \leftrightarrow NiOOH(III) + e^- \quad (10)$$

3.3. *Electrochemical properties of the hybrid supercapacitor device assembled by Zn–Ni–Co MOF (Zn-3) and active carbon*

Zn-3 had the best electrochemical performance in a three-electrode system. Therefore, Zn-3 was used as the positive electrode and AC as the negative electrode to study the electrochemical performance of Zn-3 in a hybrid supercapacitor (HSC), 6 M KOH aqueous as electrolyte (Fig. 6a). The electrochemical properties of AC in a three electrode system was performed in Fig. S11. Fig. S11a shows the CV cures at scan rates from 5 mV/s to 50 mV/s, and Fig. S11b shows the GCD curves at current densities from 1 A/g to 20 A/g. A voltage window from −1.1 V to 0 V was selected in AC, and a voltage window from 0 V to 1.5 V in HSC was roughly estimated from this, since there is no overlap between AC's voltage window and Zn-3's voltage window (Fig. 6b). Fig. 6c presented the CV curves of Zn-3//AC HSC at scan rates from 5 mV/s to 50 mV/s over a voltage range from 0 V to 1.5 V. redox peaks present at about 1.1V and a smooth curves in 0V–0.9 V confirms that the energy storage mechanism of this HSC contains both double electric layer and pseudocapacitance. Fig. 6d shows the GCD curves of Zn-3//AC HSC at current densities of 1 A/g to 20 A/g. The GCD curves of the HSC maintain a good symmetry under high current densities, which prove that the redox reaction in energy storage process is reversible and that the device has a good Coulombic efficiency.

The cyclic stability and the Coulombic efficiency of Zn-3//AC HSC was tested under the current density of 10 A/g. As shown in Fig. 6e, After 3000 cycles, the retention of HSC's capacitance maintain about 60 %, and the Coulombic efficiency was about 100 %. The first and the last 10 cycles of the cycling stability performance test was shown in Fig. S11c and S11d respectively. Furthermore, to verify the practical application performance of Zn-3//AC HSC, we make it as the power of a small LED bulb, and the bulb stay on for several hours. Additionally, the power density and the energy density of this HSC was calculated by equations (7) and (8). This device has a energy density of 58 Wh/kg at a power density of 775 W/kg. And it still retains an energy density of 12 Wh/kg at a power density

of 7750 W/kg, which was better than graphite nanosheets decorated with Ni-MOF [28], Ni–Co MOF onto porous support [52], hierarchical NPO@CNTs derived from Ni-MOF [53] and other Ni–Co MOF derived materials [54–57]. The ragone plot correlating E and P of these hybrid devices was shown in Fig. 6f.

4. Conclusions

In summary, Ni–Co MOF was obtained by hydrothermal process, and the M-Ni-Co MOF (M = Zn, Fe, Mn) was obtained by hydrothermal process based on Ni–Co MOF with the best electrochemical performance. M-Ni-Co MOF with different morphology were made by introducing different M ions. The electrochemical performance of Zn–Ni–Co MOF was up to 1135 F/g at 1 A/g current density. In addition, Zn-3//AC hybrid supercapacitors performed a energy density of 58 Wh/kg at a power density of 775 W/kg. This study introduce a method to make MOFs with different morphology to get a better electrochemical performance, which can also be applied to other MOF materials.

CRediT authorship contribution statement

Yige Yan: Writing – original draft, Writing – review & editing, Visualization, Methodology, Investigation, Formal analysis, Data curation, Conceptualization. **Mohan Huang:** Writing – review & editing, Visualization. **Yongsheng Wang:** Supervision, Resources, Project administration, Funding acquisition. **Dawei He:** Supervision, Resources, Project administration, Funding acquisition. **Jiaqi He:** Writing – review & editing, Funding acquisition, Formal analysis.

Declaration of competing interest

The authors declare that they have no known competing financial interests or personal relationships that could have appeared to influence the work reported in this paper.

Acknowledgements

We are grateful for the financial support of the National Natural Science Foundation of China (Grant Nos. 61975007), the Beijing Natural Science Foundation (Grant No. Z190006, 4222073)

Appendix A. Supplementary data

Supplementary data to this article can be found online at https://doi.org/10.1016/j.heliyon.2024.e25586.

References

[1] B. Dunn, H. Kamath, J.-M. Tarascon, Electrical energy storage for the grid: a battery of choices, Science 334 (6058) (2011) 928–935, https://doi.org/10.1126/science.1212741.
[2] W. Zuo, R. Li, C. Zhou, Y. Li, J. Xia, J. Liu, Battery-supercapacitor hybrid devices: recent progress and future prospects, Adv. Sci. 4 (7) (2017) 1600539, https://doi.org/10.1002/advs.201600539.
[3] Ibrahim Khan, Syed Shaheen Shah, Abdulmajeed Hendi, Muhammad Ashraf, Younghyun Cho, Shahid Ali, Sanghyuk Wooh, Tailoring performance of hybrid supercapacitors by fluorine-rich block copolymer-derived carbon coated mixed-phase TiO2 nanoparticles, J. Alloys Compd. 968 (2023) 172–175. Lingcong Guo, Pan Hu, Hong Wei, Development of supercapacitor hybrid electric vehicle, Journal of Energy Storage, Volume 65, 2023.
[4] Yang Liu, Mohan Huang, Min Lu, Xiaohui Guan, Xin Guan, Guangsheng Wang, Bo Jia, Facile design and synthesis of nickle-molybdenum oxide/sulfide composites with robust microsphere structure for high-performance supercapacitors, Chem. Eng. J. 364 (2019) 462–474.
[5] C. Merlet, B. Rotenberg, P.A. Madden, P.-L. Taberna, P. Simon, Y. Gogotsi, M. Salanne, On the molecular origin of supercapacitance in nanoporous carbon electrodes. Nature Materials 11 (4) (2012) 306–310, https://doi.org/10.1038/nmat3260.
[6] F. Liu, T. Wang, X. Liu, L. Fan, Challenges and Recent Progress on Key Materials for Rechargeable Magnesium Batteries. Advanced Energy Materials 11 (2) (2020) 2000787, https://doi.org/10.1002/aenm.202000787.
[7] J.P. Zheng, P.J. Cygan, T.R. Jow, Hydrous ruthenium oxide as an electrode material for electrochemical capacitors, J. Electrochem. Soc. 142 (8) (1995) 2699–2703.
[8] W. Dmowski, T. Egami, K.E. Swider-Lyons, C.T. Love, D.R. Rolison, Local atomic structure and conduction mechanism of nanocrystalline hydrous RuO2 from X-ray scattering, J. Phys. Chem. B 106 (49) (2002) 12677–12683.
[9] H. Furukawa, K.E. Cordova, M. O'Keeffe, O.M. Yaghi, The chemistry and applications of metal-organic frameworks, Science 341 (6149) (2013).
[10] O.M. Yaghi, M. O'Keeffe, N.W. Ockwig, H.K. Chae, M. Eddaoudi, J. Kim, Reticular synthesis and the design of new materials, Nature 423 (6941) (2003) 705–714.
[11] R. Freund, O. Zaremba, G. Arnauts, R. Ameloot, G. Skorupskii, M. Dincă, S. Wuttke, The current status of MOF and COF applications, Angew. Chem. Int. Ed. (2021).
[12] Z.W. Zhu, Q.R. Zheng, Investigation of cryo-adsorption hydrogen storage capacity of rapidly synthesized MOF-5 by mechanochemical method, Int. J. Hydrogen Energy 48 (Issue 13) (2023) 5166–5174.
[13] David Ursueguía, Eva Díaz, Salvador Ordóñez, Metal-Organic Frameworks (MOFs) as methane adsorbents: from storage to diluted coal mining streams concentration, Sci. Total Environ. 790 (2021).
[14] Zhanke Wang, Lei Ge, Mengran Li, Rijia Lin, Hao Wang, Zhonghua Zhu, Orientated growth of copper-based MOF for acetylene storage, Chem. Eng. J. 357 (2019) 320–327.
[15] Naef A.A. Qasem, Rached Ben-Mansour, Mohamed A. Habib, An efficient CO2 adsorptive storage using MOF-5 and MOF-177, Appl. Energy 210 (2018) 317–326.

[16] Mohan Huang, Kun Zhao, Zhiying Bai, Dawei He, Jiaqi He, Yongsheng Wang, Both MOFs-derived Fe-Co-Ni ternary hydroxide positive and Fe2O3/reduced graphene oxide negative electrode for asymmetric supercapacitors, J. Colloid Interface Sci. 623 (2022) 1160–1171.
[17] Yuxia Xu, Qing Li, Xiaotian Guo, Songtao Zhang, Wenting Li, Huan Pang, Metal organic frameworks and their composites for supercapacitor application, J. Energy Storage 56 (2022). Part A.
[18] Jia-Wei Wang, Ying-Xia Ma, Xiao-Ya Kang, Hai-Jun Yang, Bing-Lu Liu, Shu-Shu Li, Xiao-Dan Zhang, Fen Ran, A novel moss-like 3D Ni-MOF for high performance supercapacitor electrode material, J. Solid State Chem. 309 (2022).
[19] Yu Han, Chuanyao Liu, Wenzhe Yue, Aisheng Huang, One-pot synthesis of conductive polypyrrole incorporated ZIF-67 for high- performance supercapacitors, Mater. Lett. 318 (2022).
[20] Xiaoya Kang, Jiawei Wang, Yingxia Ma, Xiaofeng Shi, Xinquan Chen, Tian Hu, Fen Ran, 3D juniperus sabina-like Ni/Co metal-organic framework as an enhanced electrode material for supercapacitors, J. Solid State Chem. 310 (2022).
[21] Q. Qian, Y. Li, Y. Liu, L. Yu, G. Zhang, Ambient Fast Synthesis and Active Sites Deciphering of Hierarchical Foam-Like Trimetal–Organic Framework Nanostructures as a Platform for Highly Efficient Oxygen Evolution Electrocatalysis. Advanced Materials 31 (23) (2019) 1901139, https://doi.org/10.1002/adma.201901139.
[22] Mohan Huang, Yue Wang, Jiangchun Chen, Dawei He, Jiaqi He, Yongsheng Wang, Biomimetic design of Ni Co LDH composites linked by carbon nanotubes with plant conduction tissues characteristic for hybrid supercapacitors, Electrochim. Acta 381 (2021).
[23] S. Jia, J. Wei, B.X. Gong, Z.Q. Shao, J. Colloid Interface Sci. 601 (2021) 640–649.
[24] Yu Xiang Liu, Qiao Jing Lin, Fei Fei Dai, Yan Xue Xue, Ding Ling Gao, Jian Hua Chen, Wei Wei Lin, Qian Yang, Efficient adsorptive removal of dibenzothiophene from model fuels by encapsulated of Cu^{+} and phosphotungstic acid (PTA) in Co-MOF, J. Solid State Chem. 321 (2023).
[25] Chao Feng, An Qi, Qiang Zhang, Lijun Huang, Nana Wang, Xiao Zhang, Yanchao Xu, Meng Xie, Ran Wang, Jiao Yang, Jianrong Chen, Unleashing the potential of Ru/FeCo-MOF in water splitting and supercapacitors through Morphology and electronic structure control, Int. J. Hydrogen Energy 55 (2024) 189–198, https://doi.org/10.1016/j.ijhydene.2023.11.134. ISSN 0360-3199.
[26] Q. Wang, L. Shang, R. Shi, X. Zhang, Y.F. Zhao, G.I.N. Waterhouse, L.Z. Wu, C.H. Tung, T.R. Zhang, Adv. Energy Mater. 7 (2017) 7.
[27] Afsaneh Karimi, Ali A. Ensafi, B. Rezaei, Design and fabrication of MOF-derived leaf-like Zn-Co-S nanosheet arrays decorated with Ni-Zn-P ultrathin nanostructure for hybrid supercapacitors, Fuel ume 334 (2023). Part 1.
[28] Jia-Wei Wang, Tian-Li Meng, Ying-Xia Ma, Lei Lei, Li Jing, Fen Ran, Fabrication of graphite nanosheets decorated with Ni-MOFs for high performance supercapacitor electrode materials, Diam. Relat. Mater. 139 (2023).
[29] Z.Y. Hu, Y.D. Miao, X.L. Xue, B. Xiao, J.Q. Qi, F.X. Wei, Q.K. Meng, Y.W. Sui, Z. Sun, J.L. Liu, J. Colloid Interface Sci. 599 (2021) 34–45.
[30] H.J. Wei, J. Liu, Y. Liu, L. Wang, L.L. Li, F. Wang, X.Y. Ren, F.Z. Ren, Compos. Commun. 28 (2021) 7.
[31] Shujuan Lv, Ying Deng, Qian Liu, Ziqi Fu, Xiaobin Liu, Minghui Wang, Zhenyu Xiao, Bin Li, Lei Wang, Carbon-quantum-dots-involved Fe/Co/Ni phosphide open nanotubes for high effective seawater electrocatalytic decomposition, Appl. Catal. B Environ. 326 (122403) (2023), https://doi.org/10.1016/j.apcatb.2023.122403. ISSN 0926-3373.
[32] Ranran Bu, Yonglong Wang, Yu Zhao, Zhenyu Xiao, Xuping Jia, Qi Zhang, Yanyan Li, Chao Chen, Lei Wang, "One-for-two" strategy: the construction of high performance positive and negative electrode materials via one Co-based metal organic framework precursor for boosted hybrid supercapacitor energy density, J. Power Sources 541 (231689) (2022), https://doi.org/10.1016/j.jpowsour.2022.231689. ISSN 0378-7753.
[33] M.J. Xie, M. Zhou, Y. Zhang, C. Du, J. Chen, L. Wan, J. Colloid Interface Sci. 608 (2022) 79–89.
[34] L.L. Song, C.L. Peng, F. Yang, L. Wang, Y.H. Jiang, Y.Q. Wang, A.C.S., Appl, Energ. Mater. 4 (2021) 4654–4661.
[35] S. Rezaee, S. Shahrokhian, Nanoscale (2020), https://doi.org/10.1039/D0NR04616G.
[36] J.T. Zhang, L. Yu, Y. Chen, X.F. Lu, S.Y. Gao, X.W. Lou, Adv. Mater. 32 (2020) 6.
[37] Yaqi Wu, Ying Deng, Jiaxin Zhang, Shujuan Lv, Zhenyu Xiao, Lu Liu, Xiaoping Jia, Chao Chen, Zhenhua Dang, Zhenjiang Li, Lei Wang, Construction of multi-channel basic cobalt/nickel phosphate core-shell microsphere for superior hybrid Zn-based supercapacitor performances, Chem. Eng. J. 455 (2) (2023) 140953, https://doi.org/10.1016/j.cej.2022.140953. ISSN 1385-8947.
[38] W.J. Song, X. Teng, Y.L. Niu, S.Q. Gong, X.M. He, Z.F. Chen, Chem. Eng. J. 409 (2021) 9.
[39] H.W. Nesbitt, D. Banerjee, Interpretation of XPS Mn(2p) spectra of Mn oxyhydroxides and constraints on the mechanism of MnO2 precipitation, Am. Mineral. 83 (3–4) (1998) 305–315.
[40] Bucket Effect, A Metal−Organic framework derived HighPerformance FeS2/Fe2O3@S-rGO negative material for enhanced overall supercapacitor capacitance, ACS Appl. Energy Mater. 4 (10) (2021) 11004–11013.
[41] H.T. Ren, S.Y. Jia, S.H. Wu, et al., Abiotic oxidation of Mn(II) induced oxidation and mobilization of As(III) in the presence of magnetite and hematite, J. Hazard Mater. 254–255 (2013) 89–97.
[42] A. Mesbah, P. Rabu, R. Sibille, S. Lebègue, T. Mazet, B. Malaman, M. François, From hydrated Ni3(OH)2(C8H4O4)2(H2O)4 to anhydrous Ni2(OH)2(C8H4O4): impact of structural transformations on magnetic properties, Inorg. Chem. 53 (2) (2014) 872–881, https://doi.org/10.1021/ic402106v.
[43] F.T. Ran, X.Q. Xu, D. Pan, Y.Y. Liu, Y.P. Bai, L. Shao, Ultrathin 2D metal-organic framework nanosheets in situ interpenetrated by functional CNTs for hybrid energy storage device, Nano-Micro Lett. 12 (2020) 1–13.
[44] Z.-L. Huang, M. Drillon, N. Masciocchi, A. Sironi, J.-T. Zhao, P. Rabu, P. Panissod, Ab-initio XRPD crystal structure and giant hysteretic effect (Hc= 5.9 T) of a new hybrid terephthalate-based cobalt(II) magnet, Chem. Mater. 12 (9) (2000) 2805–2812.
[45] S.S. Zheng, B. Li, Y.J. Tang, Q. Li, H.G. Xue, H. Pang, Ultrathin nanosheet-assembled [Ni3(OH)2(PTA)2(H2O)4]•2H2O hierarchical flowers for high-performance electrocatalysis of glucose oxidation reactions, Nanoscale 10 (2018) 13270–13276.
[46] D.D. Liu, C.Q. Yi, D.W. Zhang, J.C. Zhang, M.S. Yang, Inhibition of proliferation and differentiation of mesenchymal stem cells by carboxylated carbon nanotubes, ACS Nano 4 (2010) 2185–2195.
[47] ACS Appl. Mater. Interfaces 9 (48) (2017) 41827–41836.
[48] ACS Nano 13 (6) (2019) 7024–7030.
[49] Zhenyu Xiao, Ben Xu, Shiyu Zhang, Zhendong Yang, Yingjie Mei, Weidong Fan, Minghui Zhang, Liangliang Zhang, Daofeng Sun, Balancing crystallinity and specific surface area of metal-organic framework derived nickel hydroxide for high-performance supercapacitor, Electrochim. Acta 284 (2018) 202–210, https://doi.org/10.1016/j.electacta.2018.07.173. ISSN 0013-4686.
[50] Jiaxin Zhang, Ying Deng, Yaqi Wu, Zhenyu Xiao, Xiaobin Liu, Zhenjiang Li, Ranran Bu, Qi Zhang, Wei Sun, Lei Wang, Chemically coupled 0D-3D hetero-structure of Co9S8-Ni3S4 hollow spheres for Zn-based supercapacitors, Chem. Eng. J. 430 (2) (2022), https://doi.org/10.1016/j.cej.2021.132836, 132836, ISSN 1385-8947.
[51] ACS Appl. Energy Mater. 3 (6) (2020) 5628–5636.
[52] S. Salehi, M.H. Ehsani, M. Aghazadeh, Direct electrosynthesis of Ni-, Co-, and Ni,Co-MOF onto porous support for high-performance supercapacitors, J. Alloys Compd. 940 (2023).
[53] Jiaxi Xu, Hao Guo, Yuan Chen, Yang Fan, Yanrui Hao, Jiaying Tian, Yinsheng Liu, Zongyan Lu, Xiaoqin Wei, Yang Wu, In-situ construction of hierarchical NPO@CNTs derived from Ni-MOF as ultra-high energy storage electrode for battery-type supercapacitor, J. Energy Storage 68 (2023).
[54] Wei Cao, Wenjing Zhao, Chenhan Xiong, Qiang Long, Nan Chen, Guoping Du, NiCo-MOF derived nanostructured NiCo-LDH@Ni(OH)2 heterogeneous composite as electrode material for hybrid supercapacitors, J. Energy Storage 64 (2023).
[55] Fateme Parsapour, Mehdi Pooriraj, Morteza Moradi, Vahid Safarifard, Shaaker Hajati, Synthesis of M/Al (M = Co, Ni, Zn) layered double hydroxide derived from aluminum fumarate-based MOF as advanced materials for supercapacitor, Synth. Met. ume 292 (2023).
[56] Peng Liu, Yuxiang Bao, Ranran Bu, Wenlu Wang, Jiaxin Zhang, Zhenyu Xiao, Xuemei Sun, Qi Zhang, Shaoxiang Li, Lei Wang, Rational construction of MOF derived hollow leaf-like Ni/Co(VO3)x(OH)2-x for enhanced supercapacitor performance, Appl. Surf. Sci. 533 (2020).
[57] Jinmi Tian, Aitang Zhang, Rui Liu, Weiguo Huang, Zhen Yuan, Rongkun Zheng, Di Wei, Jingquan Liu, Preparation of CoS2 supported flower-like NiFe layered double hydroxides nanospheres for high-performance supercapacitors, J. Colloid Interface Sci. 579 (2020) 607–618.